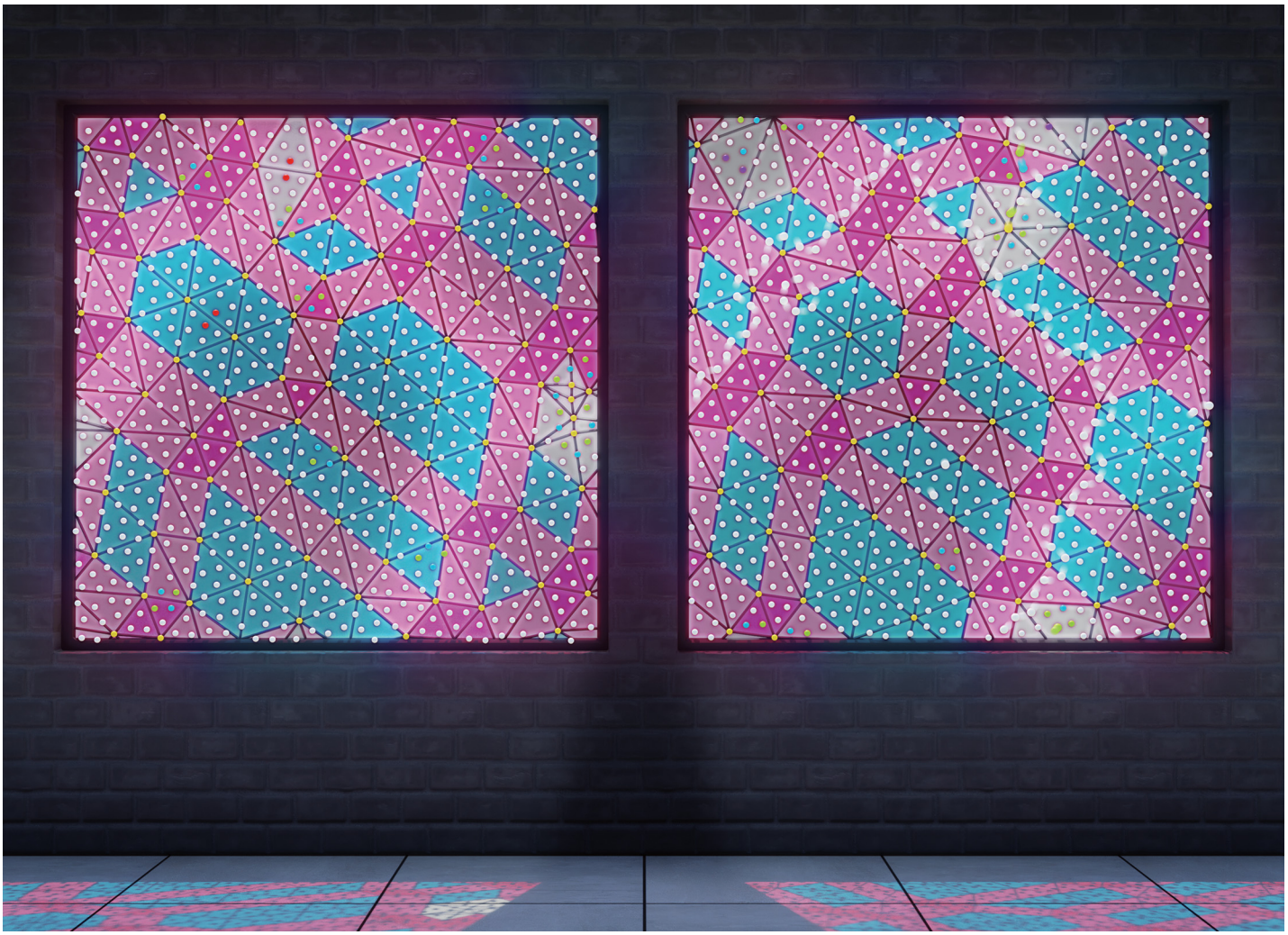

National Institute of Advanced Industrial Science and Technology (AIST) and Tohoku University, Japan.

Formation and fluctuation of two-dimensional dodecagonal quasicrystals

Particles in a dodecagonal quasicrystal are collectively displaced. The order of the structure can be seen from the particle positions after decorating the particles according to their local structures and the triangulated network. Each vertex is the centre of a dodecagonal motif made of nineteen particles. The changes in the network are associated with the displacements of chains of particles.

As featured in:

See Uyen Tu Lieu and Natsuhiko Yoshinaga, *Soft Matter*, 2022, **18**, 7497.

ROYAL SOCIETY OF CHEMISTRY

rsc.li/soft-matter-journal

Registered charity number: 207890

Soft Matter

PAPER

View Article Online
View Journal | View Issue

Cite this: *Soft Matter*, 2022, **18**, 7497

Formation and fluctuation of two-dimensional dodecagonal quasicrystals†

Uyen Tu Lieu *[a] and Natsuhiko Yoshinaga *[ab]

Received 16th June 2022,
Accepted 23rd August 2022

DOI: 10.1039/d2sm00798c

rsc.li/soft-matter-journal

The self-assembly of two-dimensional dodecagonal quasicrystals (DDQCs) from patchy particles is investigated by Brownian dynamics simulations. The patchy particle has a five-fold rotational symmetry pattern described by the spherical harmonics Y_{55}. From the formation of the DDQC obtained by an annealing process, we find the following mechanism. The early stage of the dynamics is dominated by hexagonal structures. Then, nucleation of dodecagonal motifs appears by particle rearrangement, and finally the motifs span the whole system. The transition from the hexagonal structure into the dodecagonal motif is coincident with the collective motion of the particles. The DDQC consists of clusters of dodecagonal motifs, which can be classified into several packing structures. By the analyses of the DDQC under fixed temperature, we find that the fluctuations are characterised by changes in the network of the dodecagonal motifs. Finally we compare the DDQCs assembled from the patchy particle system and isotropic particle system. The two systems share a similar mechanism of the formation and fluctuation of DDQCs.

1 Introduction

Quasicrystals (QCs) are ordered structures lacking periodic translational symmetry.[1,2] Different from crystals which possess 2-, 3-, 4-, and 6-fold rotational symmetry, QCs may have 5-, 8-, 10-, 12-, and 18-fold rotational symmetry. QCs can be applied in various applications, such as advanced coatings, reinforced composites, optics, photovoltaics, magnetism,[3] superconductivity,[4] and bandgap materials in photonic devices.[5] The appearance of QCs and approximants has been observed in different length scales, from intermetallics[1,6] to meso-scale.[7–11] Recently, quasicrystalline structures have been found in soft materials, such as block copolymers,[12,13] surfactants,[14] colloids,[15] and dendrimers.[16]

The quasiperiodic self-assembly has been obtained mainly by three types of mechanisms: isotropic interactions between particles, anisotropic interactions between particles, or polydispersity. In the first case, the isotropic interaction potential depends only on the distance between particles, but has at least two length scales.[17–22] For example, the Lennard-Jones–Gauss potentials can produce decagonal QCs or dodecagonal QCs (DDQCs),[17] or the hard-core/square-shoulder potentials[22] create a family of QC structures with 10-, 12-, 18- and 24-fold bond orientational order. Continuum description has also been proposed in ref. 23–25. The three-well oscillating pair potential is able to form a three-dimensional icosahedral QC in non-atomic systems.[18]

In the second case of anisotropic interactions between particles, the interactions depend on their mutual orientation while the distance-dependence has only one length scale. For example, the five-patch particles, whose five sticky patches are equally distributed around the equator of the sphere, can arrange into a two-dimensional DDQC;[26–29] hard tetrahedra create a three-dimensional DDQC.[30]

In the third type of systems, DDQCs and approximant structures are realised in polydisperse systems,[8,31,32] such as binary nanoparticles with two different sizes,[8] and bidisperse pentavalent and hexavalent patchy particles.[31] Recently icosahedral QCs have been built from a mixture of patchy particles.[33]

Despite intensive studies on the structural characterisation of QCs, the kinetics and dynamics of QC growth, are still incomplete.[34–37] It is not clear how the QCs appear from a liquid or crystalline state, what is happening at the periphery of QCs during their growth, and how local structures change under thermal fluctuation after QC formation. It is also of interest whether the dynamics and kinetics of QCs are dependent or not on the three aforementioned mechanisms. Most of the previous studies focused on the analysis of the structures. In ref. 26 and 27, stable DDQCs were generated *via* Monte-Carlo simulations of the five-patch particles. In ref. 28, the growth of DDQCs was studied by particle deposition on a prepared quasicrystalline substrate. The growth of a three-dimensional DDQC was studied in ref. 34, and it was suggested that characteristic structures

[a] *Mathematics for Advanced Materials-OIL, AIST, 2-1-1 Katahira, Aoba, 980-8577 Sendai, Japan. E-mail: uyen.lieu@aist.go.jp*
[b] *WPI-Advanced Institute for Materials Research (WPI-AIMR), Tohoku University, 2-1-1 Katahira, Aoba, 980-8577 Sendai, Japan. E-mail: yoshinaga@tohoku.ac.jp*

† Electronic supplementary information (ESI) available: Simulation results for isotropic particles. See DOI: https://doi.org/10.1039/d2sm00798c

(icosahedra in that system) preferentially appear around the nucleus of DDQCs. The growth of a two-dimensional DDQC was also studied in ref. 38. Nevertheless, what kind of local structures preferentially appear near the nucleus of QCs in other systems remains unknown. Also, it is of relevance to clarify how those structures are transformed as a part of DDQCs by particle displacements.

To clarify those issues, it is necessary to analyse the dynamics of local structures. We carry out the analyses in different scales: local structures based on neighbours, (dodecagonal) motifs consisting of several particles, and packing of the motifs. These structural changes have not been studied in the previous studies.

In this study, we investigate the kinetics and dynamics of DDQCs by computer simulations. The majority of reported QCs in soft materials are DDQCs. Therefore, we focus on the formation of DDQCs. We have developed a model for the interaction of a pair of anisotropic particles whose surface pattern is described by spherical harmonics Y_{lm}.[39,40] Using the five-fold symmetry patchy particles, we are able to assemble the DDQC. We investigate the formation of the DDQC from a bulk phase, and the local structural changes (fluctuation) after the DDQC is formed. The same procedure is applied to the DDQC assembled from the isotropic particle system. We compare the kinetics and dynamics of the DDQCs from the patchy particle system and the isotropic particle system.

2 Methods

2.1 Numerical simulation

We consider the patchy particle with five-fold symmetry, composed of ten alternating patches of two different types (Fig. 1). The pattern on a spherical particle is described by spherical harmonics Y_{55}.[39,40]

The pairwise interaction of the particles includes a Weeks–Chandler–Andersen (WCA) term preventing the overlap and a Morse-like, orientation-dependent term. The details of the anisotropic potential are given in Appendix A. Fig. 2 illustrates the potential used in the study at different particle configurations.

The assembly of patchy particles is performed by Brownian dynamics simulations.[41] The positions $\mathbf{r}$ and orientations $\mathbf{\Omega}$ of the particles after the time step Δt are updated according to the equations

$$\mathbf{r}(t+\Delta t) = \mathbf{r}(t) + \frac{D^{\mathrm{T}}}{k_{\mathrm{B}}T}\mathbf{F}(t)\Delta t + \boldsymbol{\delta}^{\mathrm{G}}\sqrt{2D^{\mathrm{T}}\Delta t}, \qquad (1)$$

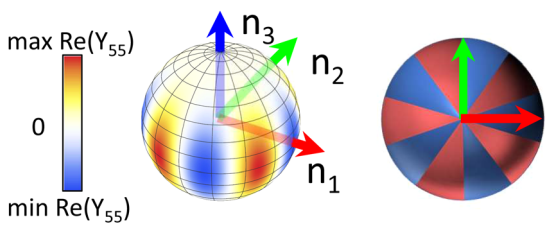

Fig. 1 Illustration of a patchy particle with five-fold symmetry expressed by the pattern of Y_{55} and the corresponding patchiness. The patches in the same colour are attractive, while those in different colours are repulsive.

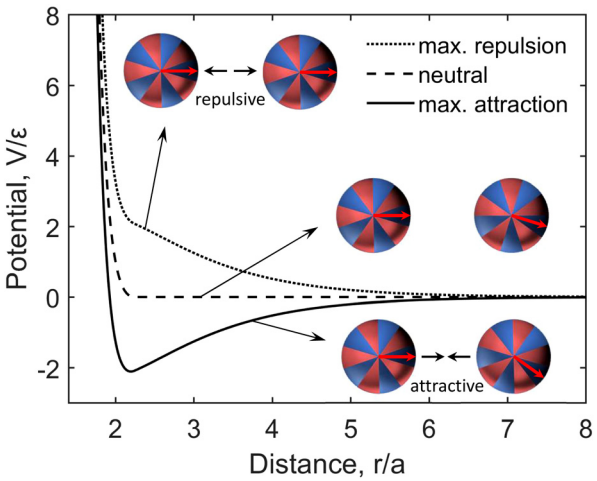

Fig. 2 Pairwise potential of patchy particles at different configurations. The red arrows indicate the orientations of the patchy particles.

$$\mathbf{\Omega}(t+\Delta t) = \mathbf{\Omega}(t) + \frac{D^{\mathrm{R}}}{k_{\mathrm{B}}T}\mathbf{T}(t)\Delta t + \boldsymbol{\delta}^{\mathrm{G}}\sqrt{2D^{\mathrm{R}}\Delta t}, \qquad (2)$$

where D^{T} and D^{R} are the translational and rotational diffusion coefficients, respectively; the force $\mathbf{F}$ and torque $\mathbf{T}$ are derived from the pair potential V; and each component of $\boldsymbol{\delta}^{\mathrm{G}}$ is a Gaussian distribution with zero mean and unit variance. The simulations are conducted in a dimensionless form where the characteristic length, energy, time, and temperature are the particle radius a, Lennard-Jones potential well-depth ε, the Brownian diffusion time $\tau_{\mathrm{B}} = a^2/D^{\mathrm{T}}$, and $\varepsilon/k_{\mathrm{B}}$, respectively.

The spherical particles are confined to a two-dimensional plane while rotating freely in three dimensions. The initial condition of the simulation is a random distribution of positions in a periodic box of size $L_x \times L_y$ with random orientations. The number of particles is $N = 1024$. The density is defined as area fraction $\rho_{\mathrm{a}} = \pi N/(L_x L_y)$.

The numerical simulations are conducted in two temperature settings: annealing and fixed temperature. In the annealing, the temperature starts from disordered states at high temperature and gradually decreases to lower temperatures at which crystalline states are stable. For the system at a fixed temperature, the system under the random initial condition is suddenly quenched at the temperature T, and the structures are relaxed at the fixed T. We choose the schedule of annealing as the temperature decreases from $T_{\max} = 1.2$ to $T_{\min} = 0.4$ with intervals of $\Delta T = 0.0125$. At each temperature the number of steps is 0.1×10^6, and the total steps are 6.5×10^6. The time step is set at $\Delta t = 0.5 \times 10^{-3}T$, and thus the total time of the annealing simulation is $t = 2600$. We have checked that the annealing schedule is slow enough to make stable QCs.

For the system at a fixed temperature, we conduct simulations at temperature $T \in [0.5,1.1]$; the number of simulation steps is 5×10^6 and the simulation time at each temperature is $t = 2500T$.

Note that we use the term *annealing* in the sense of simulated annealing, consisting of melting and successive cooling.[42]

In our system, the initial condition is a disordered state and the initial temperature T_{max} = 1.2 is high enough to get large thermal fluctuation. Therefore, we do not need a process to increase the temperature during annealing.

To analyse the fluctuation of the DDQC, simulations are performed with the parameters area fraction ρ_a = 0.75, fixed temperature T = 0.8 and 50 × 10^6 steps, which are approximately 10 times longer and slightly less dense than the annealing simulations. For five independent simulations, the DDQC is formed from a rich hexagonal phase after the first 5 × 10^6 steps. The fluctuation of the DDQC is reported after it is formed. We also investigate the DDQC assembled from the isotropic interacting particles. The details of the potential and simulation condition are given in Appendix B.

2.2 Structural analysis

The types of local structures of each particle are determined by the connection of the nearest neighbours of a particle. The local environments in a DDQC are σ, H, and Z[26] as given in Fig. 3. These local structures are based on the number of common neighbours of the neighbouring particles analogous to the Frank–Kasper phases. For example, a σ particle has five neighbours. One of them has two common neighbours, and four of them have only one common neighbour. Therefore the local structure of a σ particle is identified as {21111}. The other local structures are H {22110}, Z {222222}, D_1 {22211}, and D_2 {222211}. In this study, the new local structures D_1 and D_2 result from fluctuating Z particles, where they form a diamond shape as shown in Fig. 3. A particle which does not fall into these categories is considered as undefined U. The number of unidentified particles is only $\lesssim$5% of the total number of particles in the system.

The local structure of the particle varies with time. The interchange of a given local structure to/from other local structures is determined between two consecutive snapshots different by 10^4 time steps, for each local structure. The purpose of this calculation is to identify the relevant "reaction" of the local structures during the growth of DDQCs. For example, we

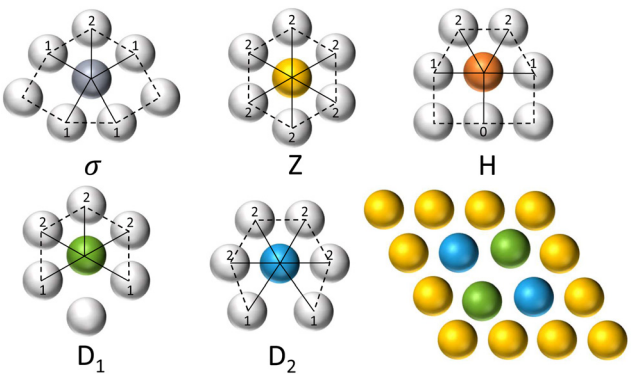

Fig. 3 Local structures σ, Z, H, D_1, and D_2 and their nearest neighbours within the distance $r \leq 2.5a$, and the illustration of the diamond structures D_1 and D_2 inside a cluster of Z particles. The number of common neighbours are also given.

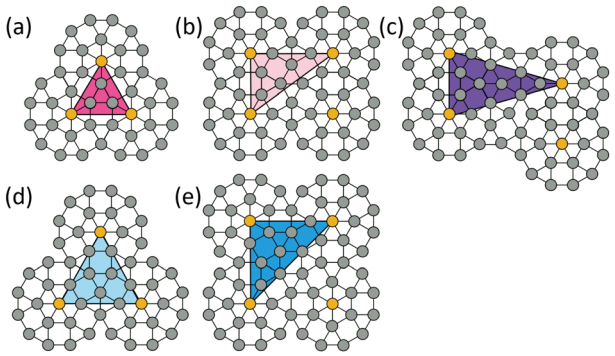

Fig. 4 Typical packing of dodecagonal motifs. The packing is characterised by the Delaunay triangulation of the dodecagonal motif centres. The yellow and grey particles are the Z and σ particles, respectively.

can calculate the interchange rate between Z and σ, which includes the amount of Z becoming σ and the amount of σ becoming Z during the two snapshots. If the amount of $Z \rightarrow \sigma$ is greater than that of $\sigma \rightarrow Z$, then the transformation of Z to σ is dominant. By the analyses of the reactions between two local structures, we may also quantify how the interchange of $Z \leftrightarrow \sigma$ (both $Z \rightarrow \sigma$ and $\sigma \rightarrow Z$) occurs more frequently than other pairs of local structures, such as $D_1 \leftrightarrow D_2$.

The DDQC has a characteristic dodecagonal motif[7,27] (see Fig. 5(e)). The motif is made of one Z particle at the centre, six σ particles on the first ring, and twelve σ particles on the second ring. Fig. 4 shows several ways of packing the motifs. These dodecagonal motifs are identified by the network of Z particles in each snapshot of simulations. The Z particles are the centres of each dodecagonal ring. We describe the motif packing by the triangular tiles in the network of Z particles obtained from Delaunay triangulation. Different clusters of motifs are shown in different colours. Each cluster is characterised by the distance between the centres of the dodecagonal motifs. For example, the dodecagonal motifs can interpenetrate in Fig. 4(a), share a common edge in Fig. 4(d) and (e), or connect *via* extra σ particles in Fig. 4(c). The criteria of the clusters are based on the edge lengths of the triangular tiles; *e.g.* the edge lengths of the perfect cluster in Fig. 4(a) are $l = (1 + \sqrt{3})2a$; a simulated cluster is of this type if the edge lengths l_{sim} satisfy $|l_{sim} - l| < 0.1l$. We will discuss how the structure of the clusters of motifs changes over time. The time-dependent network structure during $[t, t + \delta t]$ is visualised by overlapping the images at $[t,\ldots,t + \delta t]$ (see Fig. 11 and 12).

3 Results of the patchy particle system

3.1 The formation of the DDQC

The dynamical self-assembly using the five-fold symmetric patchy particles under annealing is investigated. Fig. 5 shows the change in the ratios of local structures during the formation of the DDQC and the representative snapshots with the colour coded according to local structures σ, Z, D_1, and D_2 (Fig. 3). Dynamical formation of a DDQC can be decomposed into three stages. At stage I, the majority of particles are Z type, with a ratio of around 0.7. The ratios of both D_1 and D_2 are around 0.1.

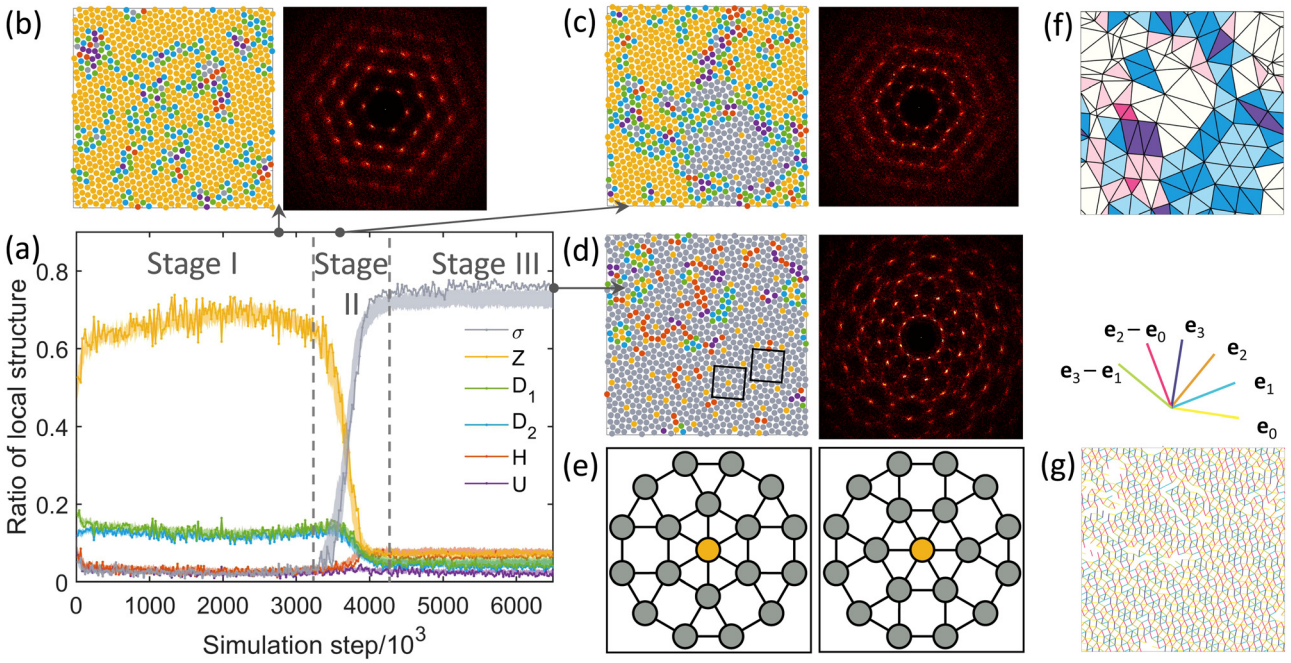

Fig. 5 Change in local structures during annealing simulations at ρ_a = 0.78. (a) Ratio of the local structure in time; the line represents the data of a simulation, and the shaded area corresponds to 95% confidence intervals of 10 independent simulations. The growth of the DDQC is divided into three stages. (b–d) The snapshots and their Fourier transformation; the colour of the particle indicates the local structure as shown in the legend and Fig. 3. (e) Illustration of two kinds of dodecagonal motifs in the boxes in (d); they are interchangeable by rotating the particles on the first ring ±30°. (f) The packing of the dodecagonal motifs of the structure in (d). (g) Orientations of the tiling edges connected by the particle positions of the structure in (d); the colours of the edges correspond to the six unit vectors shown above.

The snapshot of this stage is a *Z*-rich structure with clear hexagonal spots in its Fourier transform. The D_1 and D_2 particles often appear in pairs as a diamond shape surrounded by *Z* particles. Stage II corresponds to the growth of the QC where the ratios of *Z*, D_1, and D_2 decrease, while that of σ increases. A σ-rich region is formed in the bulk of *Z* particles. The σ-rich region contains a few *Z* particles inside. The D_1 and D_2 particles accumulate at the boundary between this region and the 'bulk' *Z* particles. Finally at stage III, when the expansion of σ reaches the system size, all the ratios maintain constant values with fluctuations. The σ-rich region spans the whole system and a DDQC is assembled, as we can observe the twelve-fold rotational symmetry in the Fourier space.[7,26]

There are several dodecagonal motifs in the QC structure. The motif contains one *Z* particle at the centre and six σ particles on the first ring and twelve σ particles on the second ring (see Fig. 5(e)). There are two types of motifs which are different by 30° degrees of the first ring. The QC structures consist of the two types of dodecagonal motifs (Fig. 5(e)) packed in different ways as shown in Fig. 4. The four structures in which the *Z* particles of the motif centres form either an equilateral triangle (Fig. 4(a) and (d)) or a right angle triangle (Fig. 4(b) and (e)) were obtained in ref. 26 using patchy particles with five-fold or seven-fold symmetry. In our simulations, aside from these packings, we also obtain the structure in which the *Z* particles form an isosceles triangle (Fig. 4(c)). Approximants can be obtained by repeating each packing structure in Fig. 4. Higher-order approximants may also be obtained by combining two or more packing types in Fig. 4, and repeating the unit structure.[31,43] DDQCs do not have any periodicity and should appear as a limit of an infinitely large unit cell. The spatial distribution of these packing structures of the dodecagonal motifs at stage III is illustrated in Fig. 5(f). There are several packing types and no periodicity in these packing types is observed.

Here, we discuss the quasicrystallinity of the obtained structures. In Fig. 5(g), a square triangle tiling whose vertices are the particles of the snapshot in Stage III is shown. The edges of the tiles are along the 12 directions at intervals of 30°. The probability of the direction of the edge along the 6 directions shown in the figure is almost identical in the range of (0.16, 0.17). This uniformity of the edge direction suggests that the structures are close to the perfect 12-fold symmetry. Next, we measure the ratio of the number of triangles to squares, and it is 983/424 ≈ 2.31 for the structure in Fig. 5(g) (it is 2.42 ± 0.065 for 10 independent snapshots). This value is comparable to the ratio $N_t/N_s = 4/\sqrt{3} \approx 2.3$ of the ideal DDQC made by inflation.[44] This ratio appears also for the random tiling of triangles and squares at maximum entropy. Finally, following the method of ref. 45 and 46, we calculate the linear phason strain tensor. To do this, we focus on the region of the well-defined square-triangle tiles in Fig. 5(g), and lift the vertices of the square-triangle tiling to 4*d* space. The perpendicular space $\mathbf{x}_\perp$ is expressed by the physical space $\mathbf{x}_\parallel$ as $\mathbf{x}_\perp = \mathbf{A}\cdot\mathbf{x}_\parallel + \mathbf{b}$, where $\mathbf{b}$ is the residual. From the invariants in the matrix $\mathbf{A}$ under rotation, we may estimate the phason strain. The obtained three invariants for the matrix of the linear phason strain

($|\alpha| \sim 0.02$, $|\beta| \sim 0.02$, and $\sqrt{\gamma^2+\mu^2} \sim 0.027$) are close to the values of the ideal dodecagonal quasiperiodic tiling ($\alpha = \beta = \sqrt{\gamma^2+\mu^2} = 0$).[45] The values of the phason strain are also far from known periodic approximants.[45] With these analyses, it is fair to call the obtained structures DDQCs, although they contain defects and are neither an ideal DDQC nor random square-triangle tiling. We should also note that the simulations are performed under the periodic boundary condition, and therefore, the size of the unit cell is bounded by the system size. In this study, by DDQCs we mean the structures discussed in this paragraph.

The ratio in Fig. 5(a), however, cannot show the "reaction" of each local structure changing to/from other local structures. Fig. 6 shows the interchange among Z, D_1, D_2, and σ. During stage I, a majority of Z particles change to and from D_1 and D_2 as the "reactions" are comparable in both forward and backward directions. In stage II, the particles Z, D_1, and D_2 change to σ faster than the backward direction. This suggests that the relevant ingredients for the formation of the σ particle, or the dodecagonal motif, are the Z, D_1, and D_2 particles.

We propose that there is a relation between Z, D_1, D_2, and σ. Specifically, the particles D_1 and D_2 play an intermediate role in the formation and expansion of the DDQC from a Z-rich

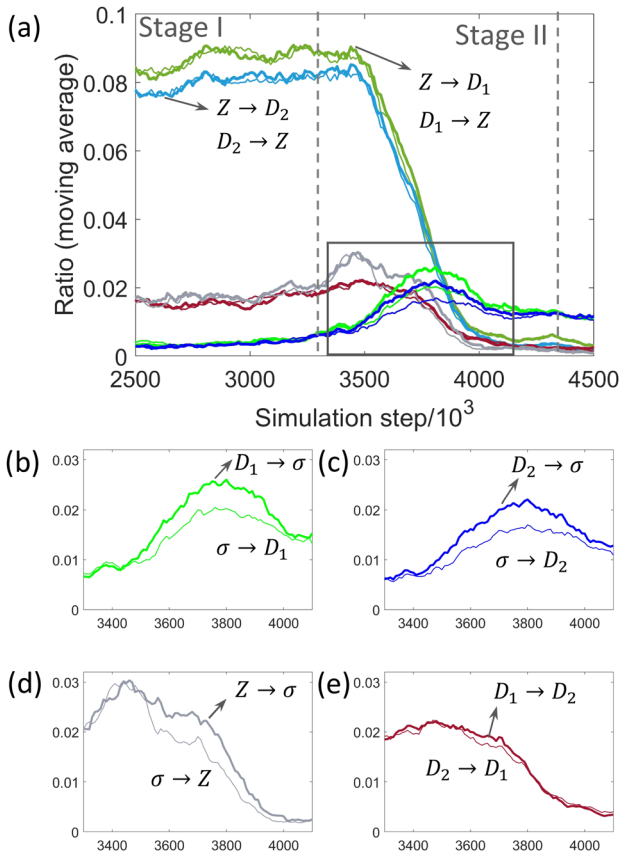

Fig. 6 Interchanges between the local structures during the growth of DDQCs at ρ_a = 0.78 by decomposition of the "in" and "out" amount of selected pairs of local structures (a). (b–e) The corresponding data inside the box in (a). The graph shows the moving average of 15 data points.

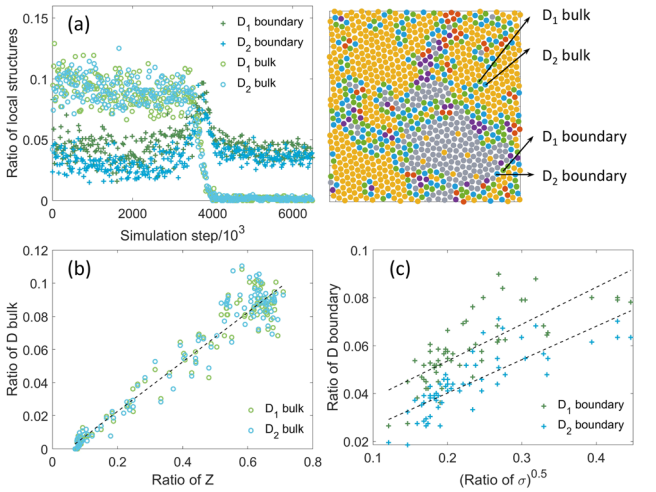

Fig. 7 Decomposition of the local structure D_1 and D_2 into the corresponding D_1 and D_2 in bulk and in boundary. (a) The composition in bulk and boundary; the illustration shows the bulk particles and the boundary particles. (b) Scaling of bulk D with Z for simulation steps [3000 × 10^3, 4100 × 10^3]. (c) Scaling of boundary D with σ for simulation steps [3000 × 10^3, 3600 × 10^3]. The dashed lines are regression data.

structure. Fig. 7(a) shows the decomposition of the D_1 and D_2 particles in terms of the bulk D_{bulk} and the boundary D_{boundary} amounts. D_{boundary} represents D particles (D_1 and D_2) neighbouring the σ particles, while the rest are defined as D_{bulk}. The bulk D fluctuates around a constant value, and then decreases to zero as the QC occupies all the space. Fig. 7(b) shows the relation between the bulk D particles and Z particles. For the bulk particles, the amount of D_1 and D_2 is almost the same as they often appear as pairs (see snapshots in Fig. 5 and 7), and linearly increases with Z. We fit the data in Fig. 7(b) by linear regression, and find the slope of 6.6^{-1}. In Fig. 3 we illustrate a diamond shape made of four D_{bulk} in twelve Z. In this case, the ratio of D_1 and D_2 to Z is equal to 6^{-1}. This argument supports a picture in which D_1 and D_2 particles appear as fluctuations of Z particles and appear in pairs.

Regarding the D particles at the boundary, as given in Fig. 7(a), these particles occupy a small amount before the growth of the σ-rich domain, then increase during the growth, and eventually decrease to a plateau. Before the QC is formed, the number of stable D particles is small and they appear stochastically associated with σ particles; then when the QC is expanded, the number of boundary D particles increases. The decrease of the boundary D is because of the limit of the finite system size. Moreover, the number of D_1 particles is higher than the number of D_2 particles, suggesting that there is extra D_1 which may contribute to the transformation from D_1 to σ or Z.

The larger number of D_1 than D_2 may be due to the anisotropy of the boundary; one side is dominated by σ particles whereas the other side is dominated by Z particles. Fig. 7(c) shows that D_{boundary} grows linearly with $\sigma^{0.5}$. This is because the growing QC has the area $\propto N_\sigma$ and the circumference $\propto \sqrt{N_\sigma}$.

We seek a simple mechanism of DDQC growth. In the simulation, the particles fluctuate locally and change their local structures continuously. However, we observe a typical local rotation of the particle during the growth of DDQCs. Fig. 8 suggests a mechanism from a Z-rich structure (stage I) to a DDQC (stage III). In the schematic of Fig. 8(a), from a hexagonal lattice, the first ring of the hexagonal lattice rotates by 15° either clockwise or anticlockwise. Simultaneously some particles of the second ring displace and eventually a dodecagonal motif is formed. The D_1 and D_2 particles also appear during this local rotation, and become σ or Z as the dodecagonal motif grows. We can calculate the rotation of the first neighbours of a centre particle (see Appendix C) from the displacements of the particles between two snapshots in Fig. 8(b). Fig. 8(c) shows that around the centres of the DDQC motif (roughly the Z particles in the DDQC), there are rotations for the particles on the first ring. The histogram in Fig. 8(d) approximately has two peaks at ±15°.

To summarise, the mechanism of the self-assembled DDQC from patchy particles can be proposed as follows: (i) initially the structure is rich in Z particles and thermal fluctuation induces the pairs of D_1 and D_2 in the bulk of Z, (ii) at the right temperature, the σ particles are formed and they cluster together to form dodecagonal motifs. (iii) The DDQC rapidly expands at the boundary where the transformation $Z \rightarrow (D_1, D_2) \rightarrow \sigma$ occurs. Around the centre of the dodecagonal motifs, local rotations of the nearest neighbours take place.

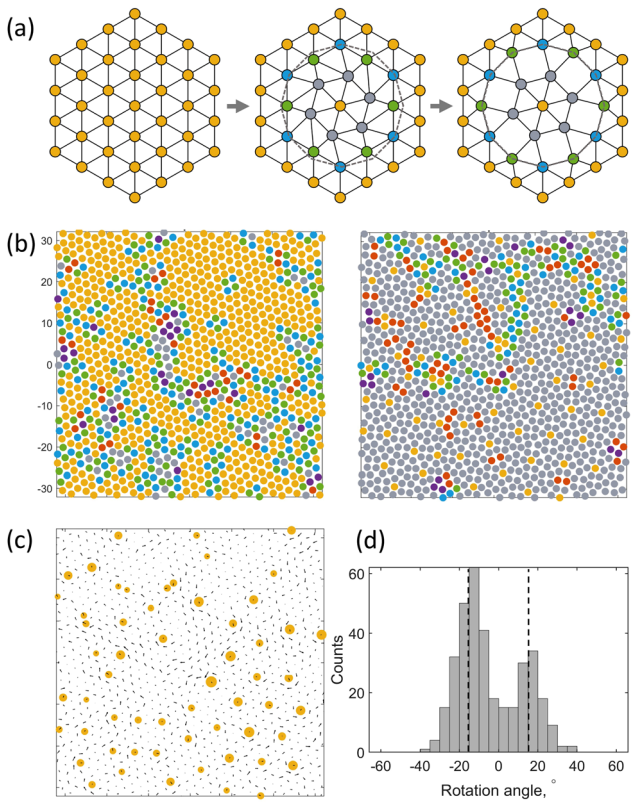

Fig. 8 Local rotation during the growth of a DDQC. (a) Illustration of local rotation from a hexagonal structure to a dodecagonal motif by rotating the particles on the first ring in the clockwise direction 15°. (b) Two snapshots before and after the DDQC is formed. (c) Corresponding displacement for the snapshots in (b). The yellow dots represent the Z particles in the DDQC. The size of Z particles indicates the "strength" of the rotation of the first ring. The Z particles of very low rotation are not shown. The displacement of the first ring of the Z particle reveals a rotation. (d) Histogram of the rotations of the neighbouring particles of the Z particles in (c). The vertical dashed lines show rotations at ±15°.

3.2 Temperature dependence of DDQC formation

In this section, the effect of temperature on the DDQC is investigated. Fig. 9 shows the dependence of the local structure ratio on temperature for annealing simulations and fixed temperature simulations. In both cases, there are two phases: Z-rich and σ-rich, separated by a critical temperature $T^* \approx 0.8$. The Z-rich phase corresponds to $T > T^*$, where the structure is dominated by Z particles and some D_1 and D_2 particles due to the strong thermal fluctuation. In this case, the global structure is hexagonal. The σ-rich region appears at $T < T^*$, where the structure is dominated by σ particles. There is a slight difference in T^* of the annealing case and the fixed temperature case. This is expected because the onset of the QC, *i.e.* the growth from the first dodecagonal motif, depends on both temperature and time, and these two parameters cannot be directly compared in the two simulation procedures. For example, at $T \approx T^*$, the onset of the annealing QC is in a uniform manner,

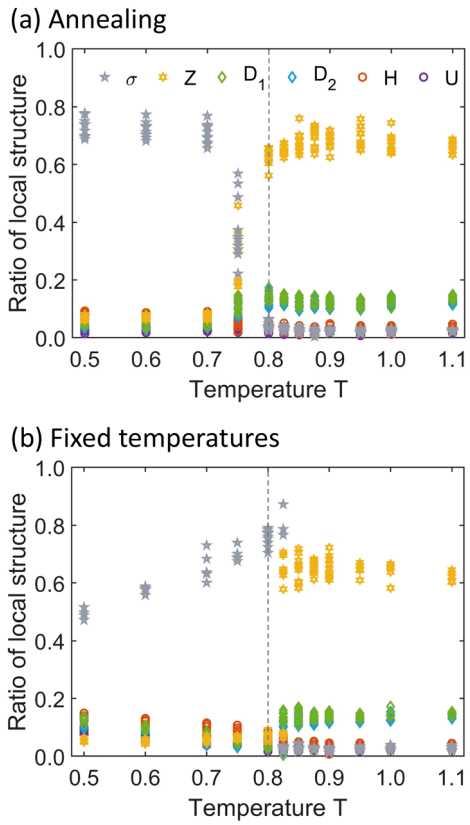

Fig. 9 Dependence of the ratio of local structure on temperature in (a) annealing simulations and (b) fixed temperature simulations at $\rho_a = 0.78$. The dashed lines estimate the critical temperature T^*.

whereas it is more scattered for the fixed temperature QC. As a result, among ten independent simulations at fixed temperature T = 0.825, three of them are DDQCs and the remaining seven are Z-rich. Regarding the quality of the QC of fixed temperature simulation, the ratio of σ particles decreases as T decreases. The fixed temperature simulation is equivalent to very fast quenching before fixing the temperature. The small ratio of σ at the low temperature is due to particles that are kinetically trapped; hence the structure is more disordered and contains more defects. Such a behaviour is not observed in the slow annealing case, as the ratio of σ is independent of temperature. The results reveal that the patchy particle DDQC can be obtained by annealing more easily than fixed temperature when $T \leq T^*$. The self-assembly of high quality DDQCs corresponds to the annealing scheme or fixed temperature at $T = T^*$.

3.3 Local fluctuation after the DDQC is formed

After the DDQC is formed, we have observed local structural changes when it is subjected to thermal fluctuation. The QC structures consist of two types of dodecagonal motifs packed in different ways as shown in Fig. 4. We focus on a network of the dodecagonal motifs, which is evaluated from the network of the Z particles because the Z particles are the centres of the dodecagonal motifs (see Section 2.2).

The structural changes are analysed by comparing snapshots at time t and $t + \delta t$. We show the change of the network in both short ($\delta t = 10^5$ in Fig. 10) and long ($\delta t = 10^6$ in Fig. 11) timescales.

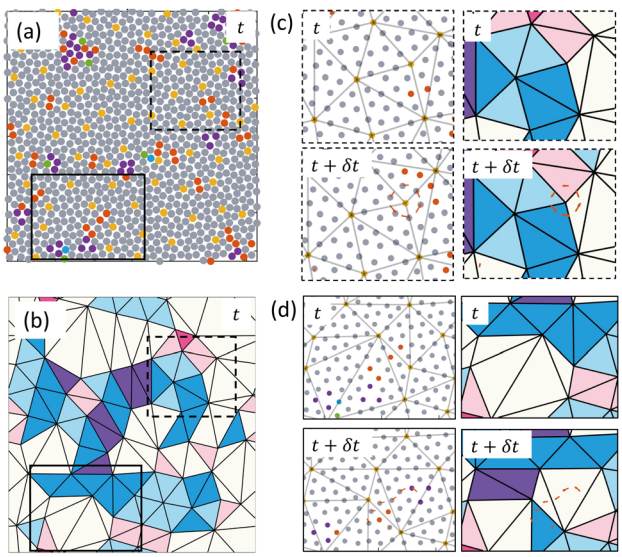

Fig. 10 Two types of changes of the dodecagonal motif network at T = 0.8. (a) A snapshot and (b) its corresponding dodecagonal motif network of Z particles at t. The coloured dots in (a) represent particle positions and particle types based on the colours in Fig. 3. Coloured triangles in (b) are different packing of dodecagonal motifs in Fig. 4. The white triangles are packing structures that cannot be classified by the structures in Fig. 4. (c and d) Change of the motif network of the boxed area in (a and b) after $\delta t = 10^5$ steps. At $t + \delta t$, the displacements of the particles from t are given by red arrows. Here, we show only the large displacements satisfying $|r(t + \delta t) - r(t)| \geq 0.5a$. For the box with a dashed line in (c), the particles rotate but the local dodecagonal network is unchanged. For the box with a solid line in (d), several particles exhibit chain-like displacement and the local dodecagonal network changes.

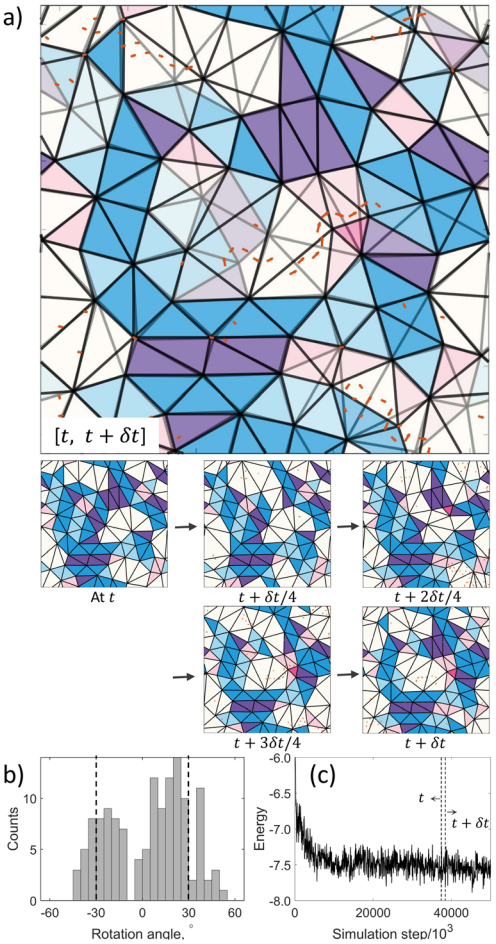

Fig. 11 Fluctuation of the dodecagonal motif network after a long time scale of $\delta t = 10^6$ steps at T = 0.8. (a) Collective movement of the particles as rearrangement of the network with superposing structures between $[t, t + \delta t]$. The small panels show the structures between $[t, t + \delta t]$. The displacements of the particles are represented by red arrows. (b) Histogram of the rotation angle of the particles in (a) with peaks at $\pm 30^\circ$ (dashed lines). (c) Energy of the whole simulation process. The windows of t and $t + \delta t$ are marked by the vertical dotted lines.

In the short timescale, Fig. 10 shows the analysed snapshot, its corresponding Z particle network by Delaunay triangulation, and two types of network rearrangement within a time scale of $\delta t = 10^5$ steps. (i) In Fig. 10(c), although a few particles move, the local motif network does not change. The displacements of these particles show that the whole first ring of the centre Z rotates 30° and eventually this dodecagonal motif is still maintained (see Fig. 5 for the two motifs). (ii) On the other hand, in Fig. 10(d), a few particles move and the local motif network changes. When those particles move, their local structures also change, *e.g.* σ particles become Z particles, and therefore the network of Z also alters. This process may continue as a chain. We observe that the displacements occur for the particles neighbouring Z (centre of the dodecagonal motif). The rearrangement of the network is coincident with the displacement.

We have analysed the phason strain using the same method as in Section 3.1. The phason strain changes by the change of the local structure in Fig. 10(d); for example, one invariant of the phason strain $|\beta|$ changes ≈ 0.02. This change is significant compared with the error in the evaluation of the phason strain $\lesssim 0.001$ when the network rearrangement does not occur. The results suggest that the change of the network is associated with phason flips.

In Fig. 11, we show the fluctuation of the dodecagonal motif network observed in a longer time scale ($\delta t = 10^6$ steps) by means of the packing of motifs for the whole simulated structure. The small panels in Fig. 11(a) are the structures between $[t, \delta t]$, while the big panel is the superposition of those small panels (see a video in the ESI†). In some regions, for example, bottom and left in Fig. 11(a), the network structure does not change, whereas in other regions, rearrangement of the network occurs. These snapshots are superposed in the big panel of Fig. 11(a). The deeper colour indicates that the network of Z particles is maintained. The region with lighter colours and overlapping edges indicates a network rearrangement. The network rearrangement has two features: first, there is a collective motion of the particles along the place where rearrangement of the network of the dodecagonal motifs occurs. Second, the network contains different types of packing structures of the dodecagonal motifs, and the displacements of the particles seem to occur between two different packing types. The chain of such collective motion is longer than the one in Fig. 10. The readers may refer to Fig. 12 for clearer visualisation of the maintained network and network rearrangement. We perform the same analysis of rotational displacement as in Section 3.1. The rotation angles of the displaced particles around the Z particles (centre of the dodecagonal motif) are around $\pm 30^\circ$ as depicted in Fig. 11(b). The structural change of the dodecagonal motif network is associated with the local rotation of the first neighbours of the motif's centre. Such rotations seem to appear at the border of different types of packing of dodecagonal motifs. During the structural changes associated with network rearrangement of dodecagonal motifs, the energy is fluctuating around a constant value as shown in Fig. 11(c).

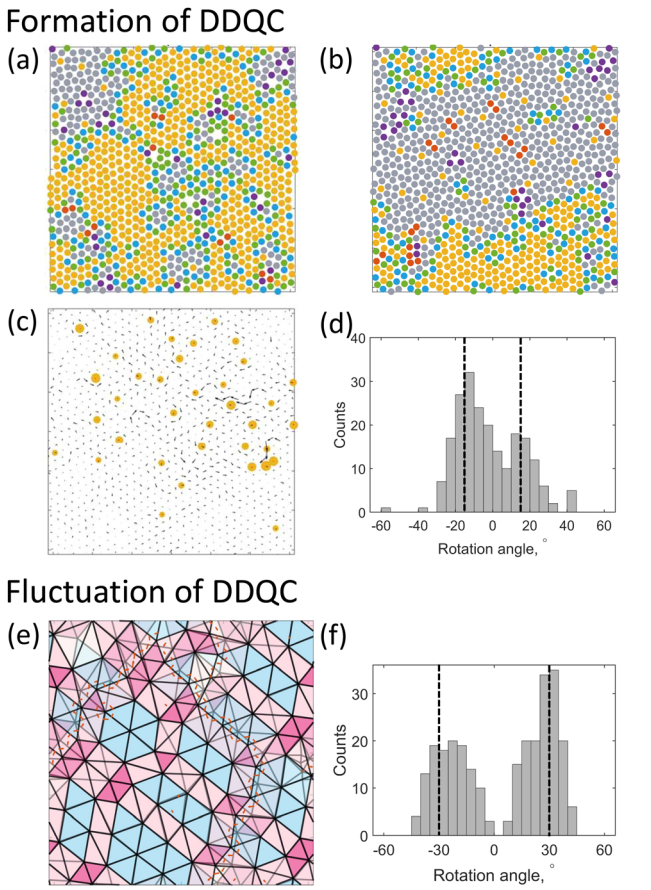

Fig. 12 Typical rotations of particles in the (a–d) formation and (e and f) fluctuation of the DDQCs. (a and b) The two snapshots for the growth of the DDQC. (c) Corresponding particle displacement of the two snapshots in (a and b). The yellow dots are the Z particles in (b). The size of Z particles indicates the "strength" of the rotation of the first ring. The Z particles of very low rotation are not shown. (d) Histogram of the rotations of the neighbouring particles of the Z particles in (c); the vertical dashed lines show rotations at $\pm 15^\circ$. (e) Change in the network of the dodecagonal motifs during the fluctuation of a DDQC. (f) Histogram of the rotation of the particles in (e); the vertical dashed lines show rotations at $\pm 30^\circ$.

4 Results of the isotropic particle system

As mentioned in the Introduction, the DDQC can be assembled also from isotropic particles. We perform the same analysis with the isotropic DDQC. The details of the potential and simulation parameters can be found in Appendix B.

Fig. 12 presents the formation and fluctuation of the isotropic DDQC. In Fig. 12(a–d), similar to the formation of the annealed patchy particle DDQC, the isotropic DDQC also starts with a Z-rich structure with some D_1 and D_2 particles generated due to fluctuation of Z. The dodecagonal motif is then organised and expanded, in which the D_1 and D_2 particles are accumulated at the boundary of the cluster of the dodecagonal motif and the Z-rich bulk. The resulting DDQC consists of dodecagonal motifs packed in different ways (Fig. 4). Regarding the mechanism of the transformation from Z-rich structures to DDQCs, the first neighbours of the dodecagonal motif centres rotate by $\pm 15^\circ$ (Fig. 12(c) and (d)). The fluctuation of the DDQC is investigated by performing simulations at a fixed temperature of $T = 0.7$. Fig. 12(e) illustrates the fluctuations of isotropic DDQCs in terms of the network of the dodecagonal motifs. The change in the network is also associated with the collective rotation by $\pm 30^\circ$ of the first neighbours of the motif centres (Fig. 12(f)). For a detailed comparison with the patchy particle system in Fig. 5, 6 and 9, the corresponding analyses for the isotropic particle system are given in Fig. S1–S3 in the ESI.†

However, there are differences between the DDQCs made of patchy particles and isotropic particles. In general, the isotropic DDQC (Fig. 12(e)) has less defects as the network has more well-defined packing structures than that of the patchy particle DDQC (Fig. 11).

In a dodecagonal motif of the DDQC, the Z particle of the isotropic system has the lowest energy whereas the energy of Z particle of the patchy particle DDQC is the highest (see Fig. 15). For the patchy particle case, the orientation of the Z particle at the centre is incompatible with the six σ neighbours. The energy of this hexagonal particle is expected to be higher than that of the σ particle, and hence σ-dominant structures are expected at low density. The patchy particle system requires fine tuning of density to assemble a DDQC, whereas the DDQC in the isotropic particle system works even under low density conditions (Fig. 16). Additional data can be found in Fig. 15 and 16 in Appendix D.

Although the DDQCs in both systems consist of dodecagonal motifs, the network of the motifs is different. In the DDQC made by the particles with the two-length-scale isotropic interaction shown in Fig. 12(e), the distance between the motifs is smaller, namely, the distance between two Z particles at the centres of two dodecagonal motifs (Fig. 5(e)) is shorter. Therefore, there are many small triangles among the packing structures, such as those of Fig. 4(a) and (b). These packing types appear less in the patchy particle DDQC, which rather consists of the packing structures of Fig. 4(c)–(e) (see Fig. 5(f) and 11(a)). We should note that the packing structures of Fig. 4(a) and (b) have triangles with shorter edges (reddish colour), whereas those of Fig. 4(d) and (e) have triangles with longer edges (bluish colour). The difference of the motif arrangement is possibly due to the potentials used in the two particle systems. As discussed above, the patchy particles prefer σ particles, whereas the isotropic particles prefer Z particles. Because Z particles are located at the centre of the dodecagonal motifs and play the role of vertices in the network of packing structures, smaller triangles tend to appear when more Z particles exist.

5 Discussion and conclusions

We have investigated the formation of DDQCs from the patchy particles with five-fold symmetry. From a Z-rich hexagonal structure, fluctuations of positions of patchy particles generate intermediate structures D_1 and D_2. After the dodecagonal motif is formed, the motif rapidly expands and the D_1 and D_2 particles are accumulated as a boundary between the cluster of the dodecagonal motif and the hexagonal structure. The DDQC contains many dodecagonal motifs packed in different ways. The formation of the DDQC is driven by the local fluctuations of the particles. The fluctuation is characterised by rotation of the first ring in the dodecagonal motif. After the DDQC is formed, the dodecagonal motif network changes when thermal fluctuation causes large displacements of the particles. The change of the network is associated with rotation of the nearest neighbours of the centres of the motifs.

Regarding the formation of the DDQC, the transformation from a Z-rich structure to a DDQC is observed in both the patchy particle system and isotropic particle system. Superposition of a hexagonal lattice and a dodecagonal motif reveals the difference in the position of the first ring, which is manifested by a circular rotation of 15° around the motif's centre. Such displacements of the particles on the first rings of the dodecagonal motifs are confirmed in our simulations. This may be the reason why the DDQCs of patchy particles and isotropic particles both share the same mechanism although the interactions are completely different.

Compared with the growth of the DDQC from a Z-rich phase in the annealing simulation, the reversal process, *i.e.* the DDQC to Z-rich phase, shows similar behaviours despite the large hysteresis in the structural transitions. A cluster of Z particles appears and then spans the whole system. Transformation from σ to Z reveals a rotation of around 15° of the first ring of the dodecagonal motif (see the schematic in Fig. 8). Further details can be found in Appendix E.

The DDQC comprises different types of packing of dodecagonal motifs (see Fig. 4). These packing structures can be constructed from the network of centres of dodecagonal motifs. The packing is divided into several characteristic structures (Fig. 4). In the obtained DDQCs, different types of packing structures coexist, and they do not show periodicity. We have observed that the DDQC continues to fluctuate in the sense that the relative positions of some particles change. Two types of displacement are considered. (i) In the case of individual displacement, the particles on the first ring of the dodecagonal motif quickly rotate. Despite the particle displacements, the whole dodecagonal motif remains intact. (ii) Collective displacement of particles can bring about rearrangement of the DDQC network. Such changes appear at the border of different types of packing structures, *i.e.* some dodecagonal motifs are disintegrated and new motifs are generated. The displacement of the particle mostly occurs at the first ring of the dodecagonal motifs, and at short length scale like (i). However such displacements can propagate to the neighbouring motifs, and the whole DDQC network eventually changes.

There is another type of DDQC made of isotropic particles[17] where the high-symmetry dodecagonal motif has five particles on the inner ring (compared to six particles for the DDQC in our study) and twelve particles on the second ring. The kinetics and dynamics of those DDQCs may be different from those in this study. We leave the analyses of such different DDQCs as a future study.

The patchy particle DDQC in our study is in agreement with other works using the five-fold symmetry patchy particle system, such as the particle with five equally distributed patches on the equator.[26] The Y_{55} patchy particle in our study also has five-fold symmetry, but the number of patches and the interaction are different. This particle has ten patches in red and blue, where the interaction of red–red/blue–blue patches is considered attractive and that of red–blue patches repulsive. In the assembled DDQC, the orientation of the patchiness of the σ particle and its neighbours (Fig. 3) is found to be similar to the one in ref. 26. Moreover, the ratios of the Z and σ particles of the DDQC in the Monte-Carlo simulations in ref. 26 are about 0.07 and 0.8, respectively, which are comparable to our system in Fig. 5.

A DDQC can be formed by a bidisperse DNA system in simulation[31] or experimentation.[32] The two DNA tiles can be considered as 5- and 6-point-star particles. The self-assembly of

the patchy particle DDQC at different densities in our study is somewhat analogical to that of bidisperse DNA systems.[32] When the ratio of the 5- to 6-point-star particle increases, the resultant structures change. A low ratio leads to σ phase structures. A medium ratio forms DDQCs of which many dodecagonal motifs are observed. At a high ratio, the hexagonal structures dominate the dodecagonal motifs. Such changes are also observed in our study when the density of the patchy particle increases.

We have investigated the formation and fluctuation of DDQCs in the patchy particle system and the isotropic particle system. It may help to predict and design the two-dimensional DDQCs in different soft matter systems. The fluctuation of the DDQC may relate to the properties of the QC, *e.g.* heat capacity. An analogical study is still required for, for example, octagonal QCs and decagonal QCs to know how the other QCs behave.

Author contributions

U. L. performed the simulations and analysed the data. N. Y. designed the research. All the authors were involved in the evaluation of the data and the preparation of the manuscript.

Conflicts of interest

There are no conflicts to declare.

Appendix

A Potential of the patchy particle system

The potential for a pair of patchy particles is

$$V = V_{\mathrm{WCA}}(r) + V_{\mathrm{M}}(r)\Xi(\mathbf{\Omega}), \tag{A1}$$

The details of the isotropic Week–Chandler–Anderson potential V_{WCA} preventing the overlapping of particles and the Morse potential V_{M} in eqn (A1) are given as

$$V_{\mathrm{WCA}} = \begin{cases} 4\varepsilon\left[\left(\frac{2a}{r}\right)^{12} - \left(\frac{2a}{r}\right)^{6} + \frac{1}{4}\right], & r \le 2a\sqrt[6]{2} \\ 0, & r > 2a\sqrt[6]{2} \end{cases} \tag{A2}$$

$$V_{\mathrm{M}} = \varepsilon M_{\mathrm{d}}\left\{\left[1 - \mathrm{e}^{\left(-\frac{r-r_{\mathrm{eq}}}{M_{\mathrm{r}}}\right)}\right]^{2} - 1\right\}, \tag{A3}$$

where $\mathbf{r} = \mathbf{r}^{ij} = \mathbf{r}^{j} - \mathbf{r}^{i}$ is the distance vector between particle centres, $r = |\mathbf{r}|$, and $\hat{\mathbf{r}} = \mathbf{r}/r$, ε is the potential well depth, r_{eq} is the Morse potential equilibrium position ($r_{\mathrm{eq}} = 1.878a$), and $M_{\mathrm{d}} = 2.294a$ and $M_{\mathrm{r}} = a$ are the Morse potential depth and range, respectively.[39,40,47]

The anisotropic interaction is calculated based on the mutual orientation of a pair of particles i and j. Let $\mathbf{n}_m^{(i)}$ and $\mathbf{n}_m^{(j)}$ with $m = 1, 2, 3$ be local bases of particles i and j, and $\hat{\mathbf{r}}$ is the unit distance vector between particle centres. The anisotropic interaction $\Xi_{lm} \propto \left\{\mathbf{C}_{(i)}^{(l,m)}\right\} \odot \nabla_{\mathbf{r}}^{2l}\frac{1}{r} \odot \left\{\mathbf{C}_{(j)}^{(l,m)}\right\}$ estimates the angular dependence of a pair of particles Y_{lm} as $\Xi_{lm} \propto \{\hat{\mathbf{n}}_0^{l-m}\hat{\mathbf{n}}_+^{m}\}_{(i)} \odot \{\hat{\mathbf{r}}^{2l}\} \odot \{\hat{\mathbf{n}}_0^{l-m}\hat{\mathbf{n}}_+^{m}\}_{(j)}$, where $\hat{\mathbf{n}}_0 = \mathbf{n}_3$ and $\hat{\mathbf{n}}_+ = \frac{1}{\sqrt{2}}(\mathbf{n}_1 + i\mathbf{n}_2)$. For example, $\Xi_{10} \propto \{\hat{\mathbf{n}}_0\}_{(i)} \odot \{\hat{\mathbf{r}}\hat{\mathbf{r}}\} \odot \{\hat{\mathbf{n}}_0\}_{(j)}$ for a pair of particles Y_{10}, and $\Xi_{20} \propto \{\hat{\mathbf{n}}_0\hat{\mathbf{n}}_0\}_{(i)} \odot \{\hat{\mathbf{r}}\hat{\mathbf{r}}\hat{\mathbf{r}}\hat{\mathbf{r}}\} \odot \{\hat{\mathbf{n}}_0\hat{\mathbf{n}}_0\}_{(j)}$ for a pair of particles Y_{20}.

B Isotropic particle system

The isotropic potential is a Lennard-Jones Gauss potential[17,19,28,48]:

$$V_{\mathrm{LJG}} = \varepsilon\left[\left(\frac{2a}{r}\right)^{12} - 2\left(\frac{2a}{r}\right)^{6} - \varepsilon' \exp\left(\frac{-(r - r_{\mathrm{G}})^2}{2(2a)^2\sigma^2}\right)\right], \tag{B1}$$

where the particle radius is a and the potential parameters r_{G}, ε', and σ^2 determine the position, depth, and width of the second well. The values of these parameters are $r_{\mathrm{G}} = 1.95 \times 2a$, $\varepsilon' = 2.0$, and $\sigma^2 = 0.02$. Fig. 13 shows the potential.

The simulation parameters are almost identical to those of the patchy particle system. The number of particles is $N = 1024$. In the annealing simulations, the temperature decreases from $T = 1.2$ to $T = 0.4$ with an interval of $\Delta T = 0.0125$. There are 100 000 steps at each value of temperature, making a total of $65 \times 100\,000$ steps.

C Determination of neighbouring rotation

The particle configuration is known at every time step. Let $\mathbf{r}(t_1)$ and $\mathbf{r}(t_2)$ be the particle position at time t_1 and t_2, respectively, and $\mathbf{d} = \mathbf{r}(t_2) - \mathbf{r}(t_1)$ the particle displacement from t_1 to t_2. Consider that the particle i has N_i nearest neighbours $\{j_1, j_2, \ldots, j_{N_i}\}$ in a clockwise order. At t_1, we define $\hat{\mathbf{e}}_{jk}$ the unit vector from j_k to j_{k+1} of the polygon made of $\{j_1, j_2, \ldots, j_{N_i}\}$. The displacement of the neighbour particle is determined from t_1 to t_2; for example, $\mathbf{d}_{j_1}$ is the displacement of the particle j_1 (Fig. 14). The rotation of the neighbours of particle i is defined as

$$\boldsymbol{\omega}_i = \frac{1}{N_i}\sum_j \mathbf{d}_{j_k} \cdot \hat{\mathbf{e}}_{j_k}. \tag{C1}$$

Note that the relative displacement to the centre particle is considered as $\mathbf{d} \mapsto \mathbf{d} - \mathbf{d}_i$.

D Energy of local structure and density dependence

We compare the energy of each local structure during the growth of the DDQC assembled from the patchy particles and isotropic particles. In each snapshot, for example, the energy of the Z

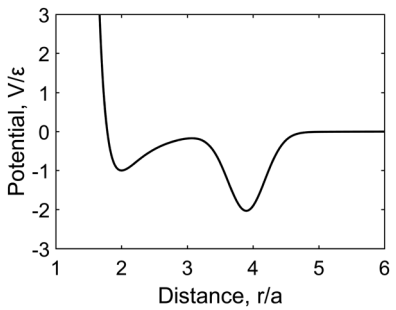

Fig. 13 Isotropic potential for the creation of a DDQC.

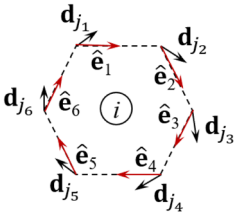

Fig. 14 Calculation of local rotation.

particle is the mean energy of all Z particles. The data are calculated from the annealing simulations of Fig. 5 and Fig. S1 in the ESI.†

The energy of each local structure during annealing is given in Fig. 15. The DDQC is steadily formed when the ratio of the local structure is in stage III. Regarding the local structure of the DDQC, the lowest energy particle is the σ particle in the patchy DDQC, while it is the Z particle in the isotropic DDQC. This is due to the difference in the two particle systems. The five-fold patchy particle prefers five nearest neighbours. Therefore, the local structure σ is expected to have the lowest energy. Then the self-assembly of patchy particles at low densities results in a σ-rich structure instead of a DDQC. In contrast, the Z particle in the isotropic DDQC has the lowest energy, and therefore the DDQC structure is formed at low densities. The decrease of energy with time when the DDQC reaches stable stage III is mainly due to lowering of temperature in annealing. As a result, the thermal fluctuation is reduced and the energy decreases.

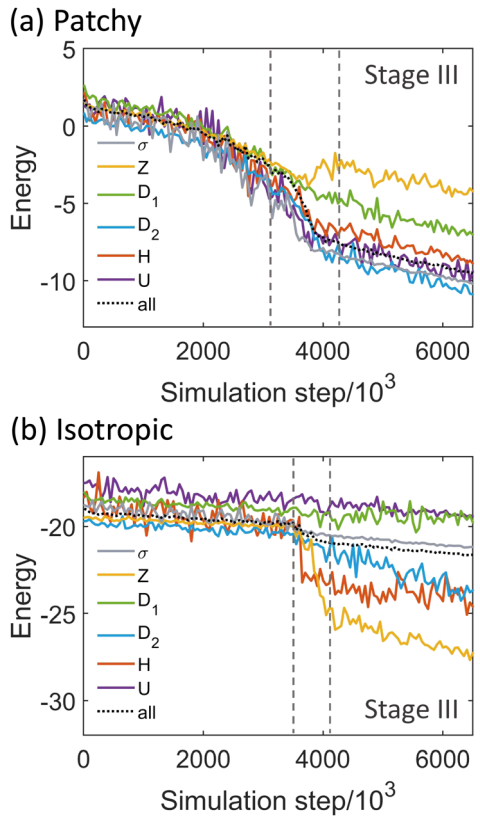

Fig. 15 Energy of local structures during annealing simulation from T = 1.2 to T = 0.4 for the (a) patchy particle system and (b) isotropic particle system. The colours of local structures are given in Fig. 3, and the black dotted line shows the average energy of all particles. The vertical dashed lines define the three stages of the growth of the DDQC (see Fig. 5).

Table 1 Parameters of annealing simulations at different densities. The results are shown in Fig. 16

	ρ_a	T_{max}	T_{min}	ΔT	Total simulation steps
Patchy particles					
(a)	0.45	1.0	0.2	0.0125	$13\,000 \times 10^3$
(b)	0.84	1.2	0.4	0.0125	6500×10^3
Isotropic particles					
(c)	0.30	1.2	0.2	0.0125	8500×10^3
(d)	0.87	1.2	0.2	0.0125	8500×10^3

We investigate the effect of density on the formation of DDQCs by patchy particles and isotropic particles. Annealing simulations are conducted at different values of the area fractions of the particles. The simulation parameters and results are given in Table 1 and Fig. 16.

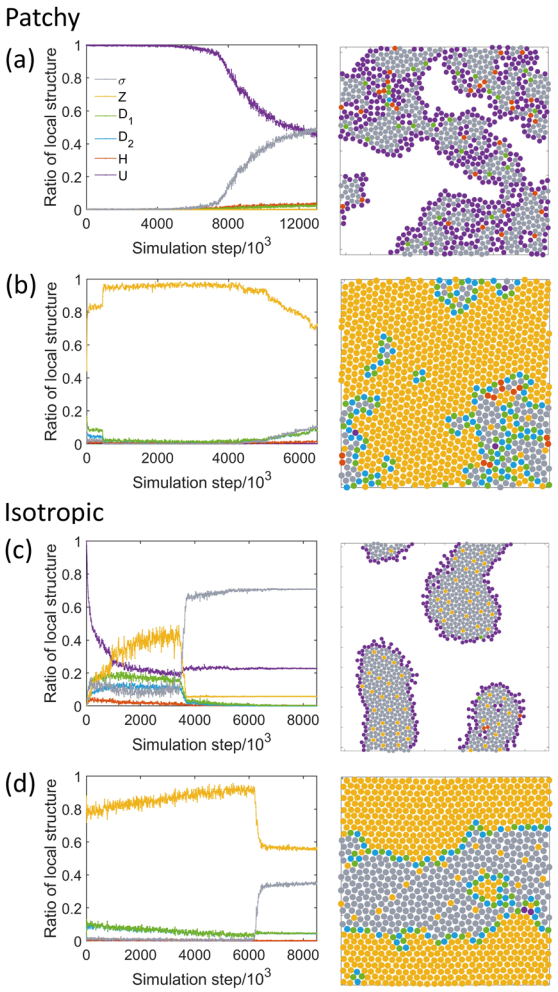

Fig. 16 Changes in the ratio of local structures of patchy particle (a and b) and isotropic particle (c and d) self-assemblies at low and high values of area fractions. The snapshots are taken at the last steps of the annealing simulations. The area fractions ρ_a of the simulations (a-d) are 0.45, 0.84, 0.30, and 0.87, respectively. The details of simulation parameters are given in Table 1.

There are different phases depending on the area fraction. For the patchy particle system, the suitable density for the assembly of the DDQC is limited around $0.69 \lesssim \rho_a \lesssim 0.81$. At low density $\rho_a < 0.69$, the structure contains clusters of σ particles and undefined particles at the interfaces. The dodecagonal motif is hardly observed (Fig. 16(a)). At high density $\rho > 0.81$ the hexagonal structure is dominant (Fig. 16(b)).

For the isotropic particle system, the DDQC more easily forms as $\rho_a \lesssim 0.84$. Even at the low density, clusters of the dodecagonal motif are clearly observed inside the interfaces (Fig. 16(c)). At high density $\rho > 0.84$ the hexagonal structure is also dominant (Fig. 16(d)).

E Structural change in the reverse process

In comparison with the growth of a DDQC from a *Z*-rich phase in the annealing simulation, the reversal process, *i.e.* the transformation of a DDQC to a *Z*-rich phase, is simulated. In this simulation, the parameters are identical to those of the annealing simulation except that the temperature is set to increase.

Fig. 17 displays the structural change and the growth of a cluster of *Z* particles for the patchy particle system. In the annealing simulation, the *Z*-rich phase transforms to a σ-rich phase at $T \sim 0.8$. In the simulation, the σ-rich phase transforms to a *Z*-rich phase at $T \sim 0.95$. Regarding the possible mechanism, in the schematic in Fig. 8 for annealing simulation, we illustrate the transformation of a hexagonal lattice to a dodecagonal motif, which can be obtained by a 15° rotation of the first neighbours of a *Z* particle. Analogically, in this reverse simulation, a region of *Z* particles is formed and then spans the whole system. At the periphery of the *Z*-rich domain, particles rotate 15°. This rotation is a reverse process of the rotation that occurs in the transformation from *Z* to σ particles for the annealing simulations. Similar hysteresis and mechanism are observed for the isotropic particle system. We also show the result in Fig. S4 in the ESI.†

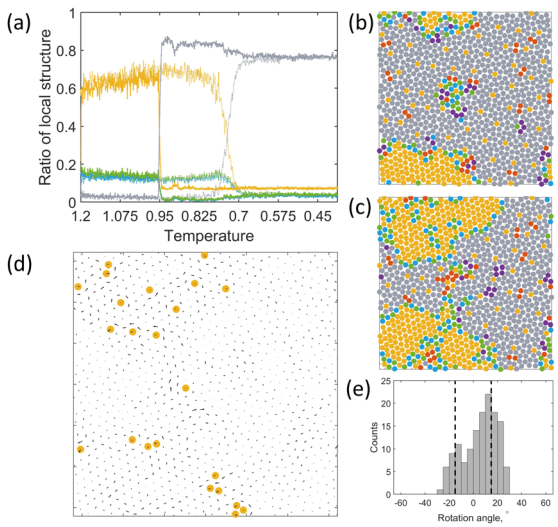

Fig. 17 The reverse transition from the DDQC to the *Z* structure for patchy particles. (a) Structural change of particle composition during the reverse (continuous line) and annealing (dotted line) processes. (b and c) Snapshots showing the expansion of the *Z* particle region during the reverse process taken at $T = 0.95$. (d) Displacements of particles from snapshot (b–c). Some rotations of the first neighbours of *Z* particles (marked yellow) can be observed. (e) Histogram of the rotation angle of the neighbours of *Z* particles in (d); the dashed lines indicate peaks at ±15°.

Acknowledgements

The authors acknowledge the support from JSPS KAKENHI Grant number JP20K14437 to U. T. L., and JP20K03874 and JP20H05259 to N. Y.

References

1 D. Shechtman, I. Blech, D. Gratias and J. W. Cahn, *Phys. Rev. Lett.*, 1984, **53**, 1951–1953.
2 D. Levine and P. J. Steinhardt, *Phys. Rev. Lett.*, 1984, **53**, 2477–2480.
3 J. I. Urgel, D. Écija, G. Lyu, R. Zhang, C.-A. Palma, W. Auwärter, N. Lin and J. V. Barth, *Nat. Chem.*, 2016, **8**, 657–662.
4 K. Kamiya, T. Takeuchi, N. Kabeya, N. Wada, T. Ishimasa, A. Ochiai, K. Deguchi, K. Imura and N. K. Sato, *Nat. Commun.*, 2018, **9**, 154.
5 W. Steurer and D. Sutter-Widmer, *J. Phys. D: Appl. Phys.*, 2007, **40**, R229–R247.
6 L. Bindi, P. J. Steinhardt, N. Yao and P. J. Lu, *Science*, 2009, **324**, 1306–1309.
7 S. Förster, K. Meinel, R. Hammer, M. Trautmann and W. Widdra, *Nature*, 2013, **502**, 215–218.
8 D. V. Talapin, E. V. Shevchenko, M. I. Bodnarchuk, X. Ye, J. Chen and C. B. Murray, *Nature*, 2009, **461**, 964–967.
9 J. Mikhael, J. Roth, L. Helden and C. Bechinger, *Nature*, 2008, **454**, 501–504.
10 T. Dotera, *Isr. J. Chem.*, 2011, **51**, 1197–1205.
11 H. Takagi, R. Hashimoto, N. Igarashi, S. Kishimoto and K. Yamamoto, *J. Phys.: Condens. Matter*, 2017, **29**, 204002.
12 A. P. Lindsay, R. M. Lewis, B. Lee, A. J. Peterson, T. P. Lodge and F. S. Bates, *ACS Macro Lett.*, 2020, **9**, 197–203.
13 K. Hayashida, T. Dotera, A. Takano and Y. Matsushita, *Phys. Rev. Lett.*, 2007, **98**, 195502.
14 K. Yue, M. Huang, R. L. Marson, J. He, J. Huang, Z. Zhou, J. Wang, C. Liu, X. Yan, K. Wu, Z. Guo, H. Liu, W. Zhang, P. Ni, C. Wesdemiotis, W.-B. Zhang, S. C. Glotzer and S. Z. D. Cheng, *Proc. Natl. Acad. Sci. U. S. A.*, 2016, **113**, 14195–14200.
15 S. Fischer, A. Exner, K. Zielske, J. Perlich, S. Deloudi, W. Steurer, P. Lindner and S. Förster, *Proc. Natl. Acad. Sci. U. S. A.*, 2011, **108**, 1810–1814.
16 X. Zeng, G. Ungar, Y. Liu, V. Percec, A. E. Dulcey and J. K. Hobbs, *Nature*, 2004, **428**, 157–160.
17 M. Engel, M. Umezaki, H.-R. Trebin and T. Odagaki, *Phys. Rev. B: Condens. Matter Mater. Phys.*, 2010, **82**, 134206.
18 M. Engel, P. F. Damasceno, C. L. Phillips and S. C. Glotzer, *Nat. Mater.*, 2015, **14**, 109–116.

19 K. Barkan, M. Engel and R. Lifshitz, *Phys. Rev. Lett.*, 2014, **113**, 098304.
20 P. F. Damasceno, S. C. Glotzer and M. Engel, *J. Phys.: Condens. Matter*, 2017, **29**, 234005.
21 M. Dzugutov, *Phys. Rev. Lett.*, 1993, **70**, 2924–2927.
22 T. Dotera, T. Oshiro and P. Ziherl, *Nature*, 2014, **506**, 208–211.
23 R. Lifshitz and D. M. Petrich, *Phys. Rev. Lett.*, 1997, **79**, 1261–1264.
24 P. Subramanian, A. J. Archer, E. Knobloch and A. M. Rucklidge, *Phys. Rev. Lett.*, 2016, **117**, 075501.
25 N. Yoshinaga and S. Tokuda, 2020, arXiv:2006.06125 [cond-mat, physics:nlin].
26 M. N. van der Linden, J. P. K. Doye and A. A. Louis, *J. Chem. Phys.*, 2012, **136**, 054904.
27 A. Reinhardt, F. Romano and J. P. K. Doye, *Phys. Rev. Lett.*, 2013, **110**, 255503.
28 A. Gemeinhardt, M. Martinsons and M. Schmiedeberg, *Eur. Phys. J. E: Soft Matter Biol. Phys.*, 2018, **41**, 126.
29 A. Gemeinhardt, M. Martinsons and M. Schmiedeberg, *EPL*, 2019, **126**, 38001.
30 K. Je, S. Lee, E. G. Teich, M. Engel and S. C. Glotzer, *Proc. Natl. Acad. Sci. U. S. A.*, 2021, **118**, e2011799118.
31 A. Reinhardt, J. S. Schreck, F. Romano and J. P. K. Doye, *J. Phys.: Condens. Matter*, 2017, **29**, 014006.
32 L. Liu, Z. Li, Y. Li and C. Mao, *J. Am. Chem. Soc.*, 2019, **141**, 4248–4251.
33 E. G. Noya, C. K. Wong, P. Llombart and J. P. K. Doye, *Nature*, 2021, **596**, 367–371.
34 A. S. Keys and S. C. Glotzer, *Phys. Rev. Lett.*, 2007, **99**, 235503.
35 W. Steurer, *Acta Crystallogr., Sect. A: Found. Adv.*, 2018, **74**, 1–11.
36 U. Grimm and D. Joseph, 1999, arXiv:cond-mat/9903074.
37 T. Janssen, G. Chapuis and M. de Boissieu, *Aperiodic Crystals*, Oxford University Press, 2018, vol. 1.
38 C. V. Achim, M. Schmiedeberg and H. Löwen, *Phys. Rev. Lett.*, 2014, **112**, 255501.
39 U. T. Lieu and N. Yoshinaga, *Soft Matter*, 2020, **16**, 7667–7675.
40 U. T. Lieu and N. Yoshinaga, *J. Chem. Phys.*, 2022, **156**, 054901.
41 M. P. Allen and D. J. Tildesley, *Computer Simulation of Liquids*, Oxford University Press, 2017, vol. 1.
42 S. Kirkpatrick, C. D. Gelatt and M. P. Vecchi, *Science*, 1983, **220**, 671–680.
43 T. Dotera, *J. Polym. Sci., Part B: Polym. Phys.*, 2012, **50**, 155–167.
44 T. Ishimasa, *Isr. J. Chem.*, 2011, **51**, 1216–1225.
45 C. Xiao, N. Fujita, K. Miyasaka, Y. Sakamoto and O. Terasaki, *Nature*, 2012, **487**, 349–353.
46 P. W. Leung, C. L. Henley and G. V. Chester, *Phys. Rev. B: Condens. Matter Mater. Phys.*, 1989, **39**, 446–458.
47 R. A. DeLaCruz-Araujo, D. J. Beltran-Villegas, R. G. Larson and U. M. Córdova-Figueroa, *Soft Matter*, 2016, **12**, 4071–4081.
48 M. Martinsons and M. Schmiedeberg, *J. Phys.: Condens. Matter*, 2018, **30**, 255403.